

STRUCTURAL, EPR AND OPTICAL STUDIES ON Cu-DOPED ZnO NANOPARTICLES SYNTHESIZED BY THE SOL-GEL METHOD AT DIFFERENT CALCINATION TEMPERATURES

ESTUDIO ESTRUCTURAL, ÓPTICO Y POR EPR DE NANOPARTÍCULAS DE ZnO DOPADAS CON Cu, SINTETIZADAS POR SOL-GEL, A DIFERENTES TEMPERATURAS DE CALCINACIÓN

ROMAN BUCHHEIT^a, F. ACOSTA-HUMÁNEZ^b Y O. ALMANZA^{b†}

a) Materials Science Department, Technische Universität Darmstadt, Building L2—01 79, Alarich-Weiss-Straße 2, 64287 Darmstadt, Germany

b) Departamento de Física, Grupo de Física Aplicada, Universidad Nacional de Colombia-Sede Bogotá, Carrera 30 No. 45-03, edificio 404, Colombia; mafacostahu@unal.edu.co, oaalmanzam@unal.edu.co[†]

† corresponding author

Recibido 3/9/2015; Aceptado 8/1/2016

In this work, pure ZnO and Cu-doped ZnO nanoparticles ($Zn_{1-x}Cu_xO$, $x = 3 \text{ at. } \%$) were synthesized using the sol-gel method at three different calcination temperatures ($T_C = 773 \text{ K}$, 823 K and 873 K). The particles were analyzed by atomic absorption spectroscopy (AAS), X-ray diffraction (XRD), electron paramagnetic resonance (EPR) at different measurement temperatures and diffuse reflection spectroscopy (DRS). All samples have wurtzite structure and the formation of a CuO was observed as additional phase. The Cu-doped nanoparticles have smaller size than the pure ZnO particles. EPR analysis shows that in samples of ZnO there is presence of superficial defects ($g = 2.036$, $g = 1.967$ and $g = 1.958$) in increased amount than in doped samples. Both samples shows Zn vacancy with $g = 2.004$. The Cu EPR signal was simulated by an anisotropic Spin-Hamiltonian with the values of $g_{\perp} = 2.082$ and $g_{\parallel} = 2.320$ and indicating that the Cu^{2+} ions in the sample have a local configuration with axial symmetry. Cu doped samples reveal a smaller band gap for the Cu-containing samples than for pure ZnO samples. Additionally, the gap of the Cu-containing samples decreases with increasing calcination temperature. Samples calcinated at 823 K are anti-ferromagnetic or ferrimagnetic at temperature lower than $T_N = 139 \text{ K}$ while samples calcinated at 873 K suffer a transition from paramagnetism to ferromagnetism which is characterized by a Curie temperature of $\Theta_C = 137 \text{ K}$.

En este trabajo fueron sintetizadas nanopartículas de ZnO puras y dopadas con Cu al 3% át. ($Zn_{0.97}Cu_{0.03}O$), a temperaturas de calcinación T_C de 773 K , 823 K y 873 K . Se hicieron análisis de espectroscopía de absorción atómica (AAS), Difracción de Rayos X (XRD), resonancia paramagnética electrónica (EPR) en función de la temperatura y reflectancia difusa (DRS). Todas las muestras tienen estructura tipo wurtzita y se observó la formación de CuO, como fase adicional. Las nanopartículas dopadas con Cu tienen menor tamaño que las no dopadas. Análisis de EPR establecen que en las muestras de ZnO hay presencia de defectos superficiales ($g = 2.036$, $g = 1.967$ y $g = 1.958$) en mayor número que las muestras dopadas. Ambas muestras muestran vacancias de Zn con $g = 2.004$. La señal EPR asociada al Cu fue simulada a partir de un Hamiltoniano anisotrópico dando valores de $g_{\perp} = 2.082$ y $g_{\parallel} = 2.320$ e indicando que el ión Cu^{2+} está en una configuración local con simetría axial. Las muestras dopadas con Cu presentan un gap electrónico menor a las muestras no dopadas. Adicionalmente es mostrado que a mayores temperaturas de calcinación, este gap disminuye. Las muestras calcinadas a 823 K tienen comportamiento anti-ferromagnético o ferrimagnético para temperaturas por debajo de $T_N = 139 \text{ K}$, mientras que las muestras preparadas a 873 K el comportamiento es ferromagnético a temperaturas por debajo de $\Theta_C = 137 \text{ K}$.

PACS: magnetic semiconductors, 75.50.Pp. sol-gel processing, 81.20.Fw. Electron paramagnetic resonance (EPR) in condensed matter, 76.30.-v. X-ray diffraction in crystal structure, 61.05.cp. Semiconductors absorption and reflection spectra of, 78.40.Fy

I. INTRODUCTION

1.1. ZnO, A Promising Material

Zinc oxide (ZnO) as a semiconductor material (gap 3.37 eV) has received much attention lately for its possible application in optoelectronics [1–4]. Since zinc oxide in its crystalline form has wurtzite type structure ($a = 0.325 \text{ nm}$ and $c = 0.521 \text{ nm}$) [1, 4], this is very stable and has properties that make it a promising material for applications in physics as gas sensor [5], solar cells [6], varistors [7] and UV-light emitting devices [8]. Its possible applications in chemistry are the use as photocatalysts [9], in medicine for its antibacterial activity [10, 11], as well as evaluating the toxicity of cancer cells [12, 13]. However, it was found that doping ZnO with

transition metals can further improve the properties of ZnO in some cases. In particular, possible applications of doped ZnO could be transparent electrodes [14], spintronics [15] or enhanced photocatalytic activity [16]. Thus, ZnO has been doped with many transition metal elements such as Co [1], Cu [2, 3, 17], Ni [18], Mn [19] and Eu [20]. These different types of metal-doped ZnO belong to the material group of diluted magnetic semiconductors (DMS), where the doping element changes the electronic, magnetic and structural properties of the ZnO matrix [1, 2, 21].

One of the interesting candidates for ZnO doping is Cu, forming $Zn_{1-x}Cu_xO$ materials. There are different preparation methods available to produce thin film or powdered forms of Cu-doped ZnO, namely the

sol-gel method [22, 23], aqueous solution method [24], auto-combustion method [20], co-precipitation method [3], mild solution method [17], and solid state reaction method [25]. These preparation methods may lead to vary material properties. For producing $Zn_{1-x}Cu_xO$ nanoparticles, the sol-gel method generally provides good material properties and exact control of the dopant concentration together with an easy synthesis process [21, 26].

1.2. Cu-doped ZnO

The research of many other groups showed that very differing electromagnetic properties were found for Cu-containing ZnO. In many cases, X-ray diffraction (XRD) and electron paramagnetic resonance (EPR) studies were used to reveal the nature of the doping material in ZnO. Elilarassi and Chandrasekaran reported successful substitution of Zn^{2+} ions by Cu^{2+} ions in the ZnO matrix, leading to ferromagnetic material properties [2]. In an earlier work, Elilarassi *et al.* explained the measured EPR signal of Cu-containing ZnO with the presence of both Cu^{2+} and Cu^{1+} in the samples [26]. Udayachandran Thampy *et al.* measured an EPR signal of Cu^{2+} ions on octahedrally distorted interstitial sites in the ZnO wurtzite structure [17]. By different spectroscopic investigations, both Jagannatha Reddy *et al.* and Elilarassi and Chandrasekaran were revealed by substituting Cu^{2+} ions on Zn^{2+} sites for their samples [4, 25]. An increase of oxygen vacancies in Cu-containing ZnO was reported by Liu *et al.* and it was explained claiming that some oxygen vacancies would be generated by Cu^{1+} substituting Zn^{2+} [21]. Finally, Elilarassi and Chandrasekaran, Udayachandran Thampy *et al.* and Liu *et al.* found also the presence of a secondary CuO phase in some of the Cu-containing ZnO samples [2, 17, 21].

The variety of results shows that generally many possibilities exist to show how the Cu can be found in Cu-containing ZnO. It is likely that magnetic properties of the material may depend on the manner of incorporation of the Cu^{2+} ions in the ZnO material. Recently, some authors have reported the synthesis and characterization of Cu^{2+} -doped ZnO nanopowders. X-ray diffraction results confirmed the presence of hexagonal wurtzite structure in their samples. From optical and EPR studies the Cu^{2+} ion occupied tetragonally distorted octahedral site symmetry [27].

This paper presents the investigation of $Zn_{1-x}Cu_xO$ nanoparticles, which were produced using the sol-gel method. Samples were calcinated at three different temperatures, so that the influence of the calcination temperature on some structural and magnetic properties will also be examined. Chemical analysis by atomic absorption made possible to determine real stoichiometry of the synthesized materials. XRD diffractograms are used for characterization of the nanoparticles and investigation of present phases in the samples. EPR measurements and simulation are done in order to contribute to the knowledge about the local configuration of the Cu ion in the samples. From results and for the first time, as far as the authors

know, it is suggested that the form in which Cu^{2+} enters the matrix can depend on the calcination temperature. So, this investigation contributes to understanding how Cu^{2+} ions may enter into ZnO matrix. Finally, band gap of powder samples is measured by diffuse reflection spectroscopy (DRS), in order to determine possible changes in the electronic structure of the samples.

II. EXPERIMENTAL

Powder samples of $Zn_{1-x}Cu_xO$ with doping molar ratio $x = 3$ at. % and undoped ZnO samples were produced using the sol-gel method. The precursors were copper(ii) nitrate trihydrate ($Cu(NO_3)_2 \cdot 3H_2O$, 99.5 % purity, Panreac), zinc(ii) nitrate hexahydrate ($Zn(NO_3)_2 \cdot 6H_2O$, 98 % purity, Panreac) and citric acid monohydrate ($C_6H_8O_7 \cdot H_2O$, 99.995 % purity, Merck). The nitrates were slowly dissolved in stoichiometric quantities in deionised water at $T = 343$ K. Stoichiometric amounts of citric acid also was dissolved in deionised water and the solution mixed with nitrates solutions at $T = 343$ K. The mixture was stirred until a gel was formed. Resulting gel was dried at $T = 403$ K for $t = 12$ h, where a temperature ramp of 1 K/min was used during heating to prevent premature crystallization. After drying, the materials were milled using an agate mortar. The powder samples of $Zn_{0.97}Cu_{0.03}O$ and ZnO were finally calcinated at different calcination temperatures $T_C = 773$ K, $T_C = 823$ K and $T_C = 873$ K using a temperature ramp of 1 K/min. The sample $Zn_{0.97}Cu_{0.03}O$ were named ZC3TTT, where 3 stands for the Cu content of $x = 3$ at. % and TTT the calcination temperature of the sample in Kelvin, i.e. ZC3873 describes the $Zn_{0.97}Cu_{0.03}O$ sample with $T_C = 873$ K. The samples of ZnO were named Z0TTT, where 0 represents the absence of doping materials. In the EPR experiments, the names of the samples are followed by three numbers, which indicate the measurement temperature, i.e. ZC3873090 means a measurement temperature of 90 K for the sample ZC3873.

Atomic absorption spectroscopy (AAS) was used for analysing chemical composition. After digestion in an aqueous solution (1:3 HCl : HNO_3), the $Zn_{1-x}Cu_xO$ samples were measured between 213.9 nm and 324.8 nm. X-ray diffraction (XRD) experiments were done for the samples with $T_C = 823$ K and $T_C = 873$ K using a Panalytical X'Pert PRO diffractometer. In the experiment, Cu- K_α radiation ($\lambda_{K_\alpha} = 0.1540598$ nm) and Bragg-Brentano configuration were used, the measurements range was from $2\theta_0 = 10^\circ$ up to $2\theta_1 = 90^\circ$ with a step size of $\Delta\theta = 0.0263^\circ$ and total counting time of the detector of $t = 97.920$ s. Lattice parameters were determined by Rietveld refinement using Fullprof [28].

The sample with $T_C = 873$ K was analyzed by Electron Paramagnetic Resonance (EPR) using a Bruker ESP 300 Spectrometer at X-band. The measurements were done with microwave frequency of $\nu = 9.44$ GHz and power microwave of $P_w = 20$ mW, with a modulation frequency of $f = 100$ kHz and a modulation amplitude of $A_m = 1.0488$ mT. The spectra was measured in a sweep width of the magnetic field $\Delta H = 500$ mT and a resolution of 4096 points per spectrum in a temperature range from $T = 90$ K up to room temperature.

Additionally to the EPR measurements, simulations were done using *MATLAB R2012b* with the *EasySpin 4.5.5* toolbox [29].

Finally, all samples were investigated by DRS using a *Varian Cary 5000* UV-vis spectrometer. The scanning interval was $\lambda_0 = 2500 \text{ nm}$ (infrared) to $\lambda_1 = 300 \text{ nm}$ (ultraviolet) with a measurement time per step of $\tau_m = 0.1 \text{ s}$ and a step interval of $\Delta\lambda = 0.1 \text{ nm}$.

III. RESULTS AND DISCUSSION

III.1. AAS Results

The real chemical composition determined by atomic absorption spectroscopy (AAS) was determined by following expression:

$$x = \frac{\eta_{Cu}}{\eta_{Zn} - \eta_{Cu}} \times 100 \% \quad (1)$$

Where x is doping molar ratio, η_{Zn} is moles of zinc and η_{Cu} moles of copper. Then, $x = 3.45 \text{ at. } \%$, $3.45 \text{ at. } \%$ and $3.44 \text{ at. } \%$ were obtained for all Cu-doped samples with $T_C = 773\text{K}$, 823K and 873K respectively. So, all samples showed a good agreement of the experimental chemical composition with the nominal value $x = 3 \text{ at. } \%$.

III.2. XRD Results

The measured XRD spectra for the samples studied are shown in Figure 1(a) and Figure 1(b).

The samples show peaks identifying ZnO in hexagonal wurtzite structure (card JCPDS 36-1451) and very low intensity peaks of copper (II) oxide (card PDF048-1548). Semiquantitative analysis was used for calculating the relative percentage of phases [30]:

$$X = \frac{A_x I_x}{A_s I_s} S \quad (2)$$

Where X is phase percentage in samples, A is mass absorption coefficient and I is apparent density for sample (x) and standard (s). Using the PDF-cards 01-089-0511 for ZnO and 98-00-0316 for CuO gives a relative percentage of the CuO phase of about 5 % in the doped samples. Scherrer's equation [31]

$$D_s = \frac{0.94\lambda_{X\text{-ray}}}{\beta \cos \Theta} \quad (3)$$

was used to determine the diameter of the nanoparticles D_s by the experimental spectra, where $\lambda_{X\text{-ray}}$ is the wavelength of the X-ray, β is the full width of half of its maximum intensity (FWHM) of the peaks and Θ is the diffraction angle of the peaks. Taken account the instrument influence to the peak broadening β_i , β was recalculated by the measured peak broadening β_m using the equation [31]

$$\beta = \sqrt{\beta_m^2 - \beta_i^2} \quad (4)$$

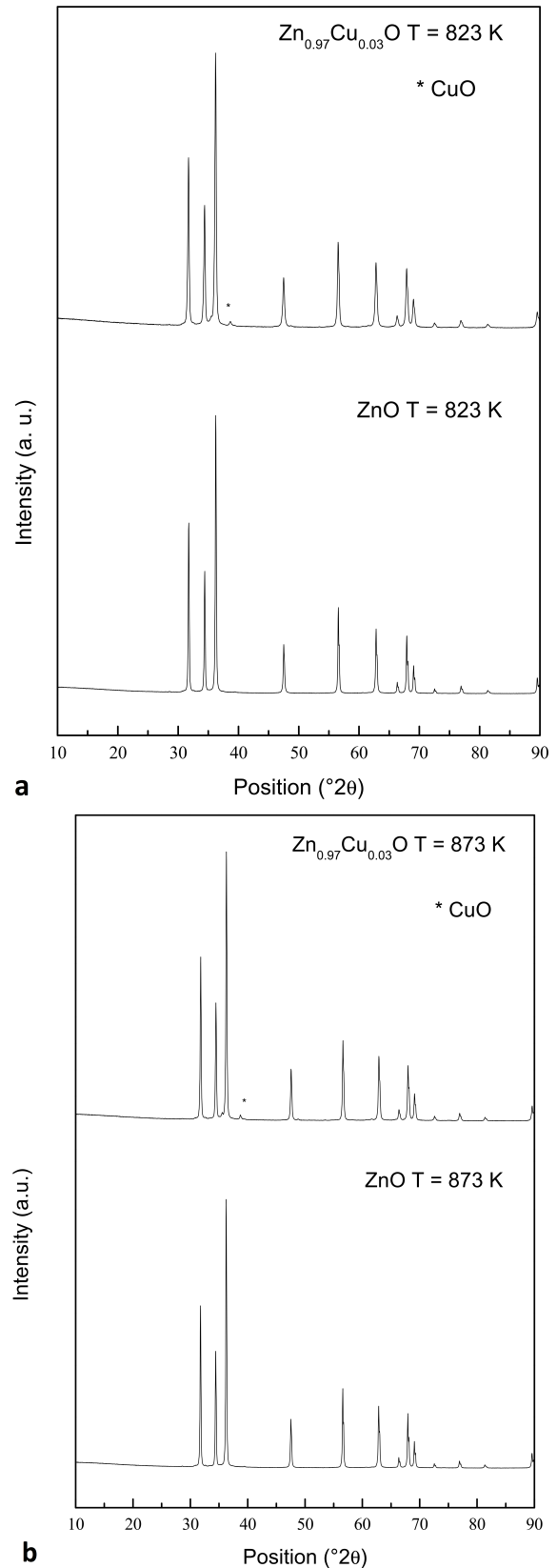


Figure 1. Measured XRD spectra for the samples calcinated at temperature of $T_C = 823 \text{ K}$ and $T_C = 873 \text{ K}$.

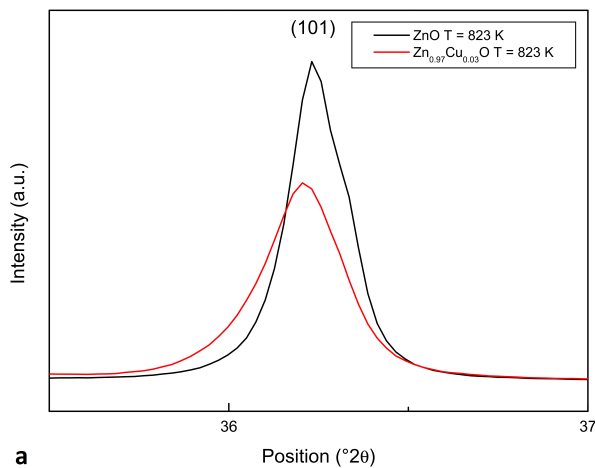
D_S was then finally determined using a linear fitting in the $1/\beta$ vs. $\cos \Theta$ plot. The results are shown in Table 1. For all T_C , the samples show a smaller particle size for ZnO with Cu-doping than for pure ZnO. This is in agreement with the observations made by other groups [2, 4, 26]. Furthermore, the particle size is smaller with increasing T_C .

Table 1. Mean particle size, D_S , was extracted from XRD data with Eq. 3. a , c and V were determined from Rietveld refinement. Strains (ϵ) were computed using Eq. 5

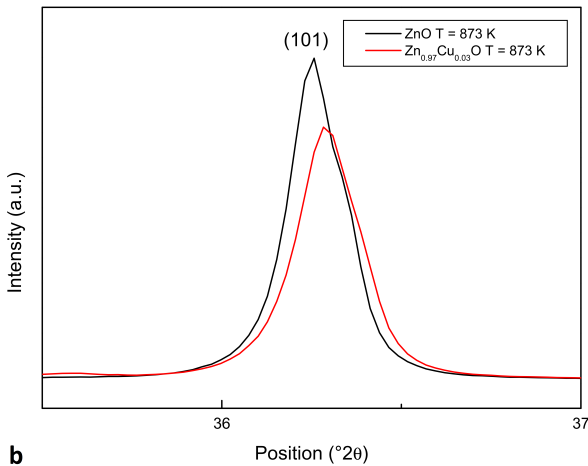
Sample	D_s (nm)	a (nm)	c (nm)	V (nm ³)	c/a	ϵ (%)
ZC3823	31.6	0.3250	0.5206	0.04763	1.602	0.0768
Z0823	35.1	0.3251	0.5208	0.04765	1.602	0.0384
ZC3873	25.3	0.3252	0.5208	0.04769	1.602	0.0384
Z0873	33.7	0.3251	0.5208	0.04766	1.602	0.0384

$$\epsilon = \frac{c - c_0}{c_0} \times 100 \% \quad (5)$$

Figure 2 shows the diffraction peaks (101) and their displacement due to introduction of Cu atoms in ZnO matrix. In Figure 2a the peak related to Cu-doped sample is shifted to the left and has lower intensity that the corresponding peak for ZnO pure.



a



b

Figure 2. XRD peaks displacement. (a) Samples calcinated at $T_c = 823$ K. (b) Samples calcinated at $T_c = 873$ K.

It could be due to microstrains generated by stoichiometric gradient since this first sample is less crystalline. In contrast,

for samples calcinated at 873 K the shifting is to the right and could be due to difference between zinc and cooper ionic radius size (Figure 2b). Microstrain values were computed using Eq. 5 [32] and are listed in Table 1.

The lattice parameters of the samples were determined by Rietveld refinement. The parameters a and c , together with the unit cell volume V , are listed in Table 1. For all samples, the c/a ratio is higher than the literature value of $c/a = 1.60$ for an ideal ZnO structure [33]. This may be explained if we accept the existence of microstrains and defects in the crystal structure. The lattice parameters and the unit cell volume is not depending on T_C or on the presence of the doping element.

III.3. EPR Results

This section presents the results of the EPR investigation of the samples with $T_C = 823$ K and $T_C = 873$ K. The EPR spectra for ZC3873 and Z0873 at $T = 90$ K are shown in Figure 3. Some of the spectra for ZC3873 measured at different temperatures are shown in Figure 4. It can be seen that the spectra changes a bit their shape, depending on the measurement temperature. At higher temperatures, a shoulder is appearing at the main drop of the Cu-signal.

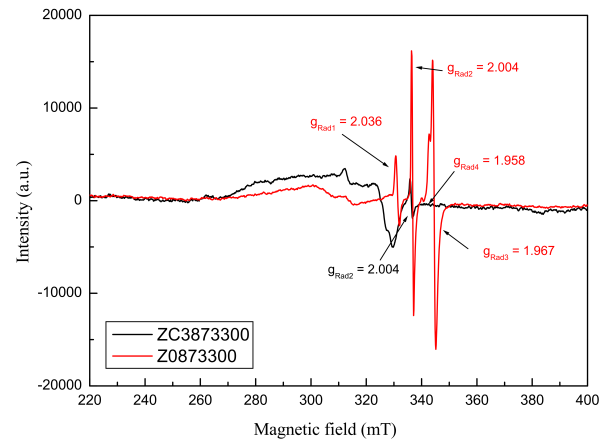


Figure 3. The EPR spectra recorded at $T = 90$ K for ZC3873 ($Zn_{0.97}Cu_{0.03}O$, black) and Z0873 (ZnO, red).

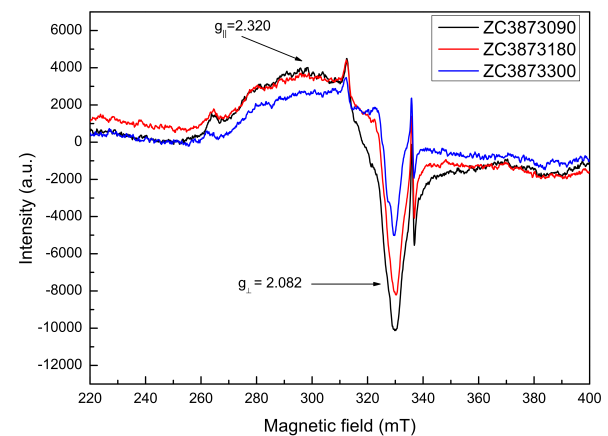


Figure 4. EPR spectra for ZC3873 measured at 90 K (black), 180 K (red) and 300 K (blue).

Z0873 shows only signals from radicals, on contrary to ZC3873, which additionally shows a signal from Cu. Figure 3 shows the g-values for the radicals measured in Z0873 and ZC3873. Z0873 shows radicals at $g_{Rad1} = 2.036$, $g_{Rad3} = 1.967$ and $g_{Rad4} = 1.958$, that are connected to shallow donors [4,34] and a radical at $g_{Rad2} = 2.004$, that is generally connected to zinc vacancies (V_{Zn}) [4,35]. ZC3873 only shows a radical at $g_{Rad2} = 2.004$.

The typical signal of Cu showed by other authors may differ slightly in shape to the spectra shown in Figure 4, as the Cu^{2+} may be in other configuration [2,4,17,25,26]. Cu EPR signal was indicated in Figure 4 made up of a smaller peak at 290.7 mT ($g_{\parallel} = 2.320$) and a bigger peak at 336.9 mT ($g_{\perp} = 2.082$). At low temperatures, an EPR spectrum is due to Cu^{2+} in axial symmetry.

The Cu EPR signal of ZC3873 was described by the Spin Hamiltonian

$$\begin{aligned} \hat{H} &= \beta_e \mathbf{H}^T \cdot \mathbf{g} \cdot \hat{\mathbf{S}} + \hat{\mathbf{S}}^T \cdot \mathbf{A} \cdot \hat{\mathbf{I}} \\ &= \beta_e \begin{pmatrix} H_x & H_y & H_z \end{pmatrix} \cdot \begin{pmatrix} g_{\perp} & 0 & 0 \\ 0 & g_{\perp} & 0 \\ 0 & 0 & g_{\parallel} \end{pmatrix} \cdot \begin{pmatrix} \hat{S}_x \\ \hat{S}_y \\ \hat{S}_z \end{pmatrix} + \\ &\quad \begin{pmatrix} \hat{S}_x & \hat{S}_y & \hat{S}_z \end{pmatrix} \cdot \begin{pmatrix} A_{\perp} & 0 & 0 \\ 0 & A_{\perp} & 0 \\ 0 & 0 & A_{\parallel} \end{pmatrix} \cdot \begin{pmatrix} \hat{I}_x \\ \hat{I}_y \\ \hat{I}_z \end{pmatrix} \quad (6) \end{aligned}$$

where β_e is the Bohr magneton, \mathbf{H}^T is the applied magnetic field, $S = \frac{1}{2}$ is the spin magnetic moment for the Cu^{2+}

ion (electronic configuration $[Ar]3d^9$), $I = \frac{3}{2}$ is the nuclear magnetic moment for the copper nuclei ^{63}Cu and ^{65}Cu and \mathbf{g} and \mathbf{A} are the g and hyperfine tensors, respectively. In Eq. 6, the Spin Hamiltonian was developed for axial symmetry of the Cu^{2+} ion.

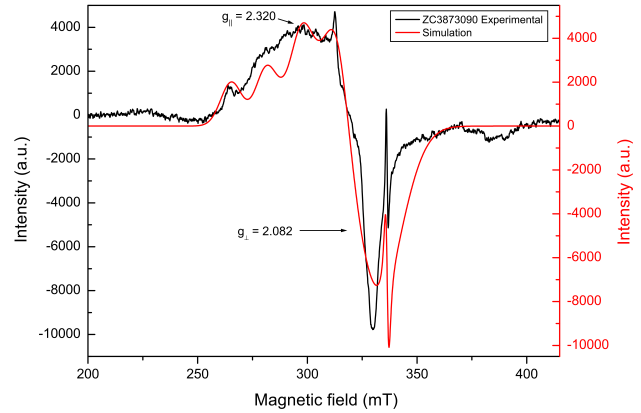


Figure 5. Experimental EPR spectra recorded at $T = 90$ K for ZC3873 (black) and the simulation, using the Hamiltonian shown in Eq. 6 and the values in Table 2 (red).

A simulation of the EPR signal together with the experimental spectrum for ZC3873 is shown in Figure 5. Radicals were also simulated using its associated experimental g-values. Table 2 shows the obtained values in the simulation, that best fits in the experimental spectra.

Table 2. Spin Hamiltonian parameters used for the simulation. The values A'_x etc. are derived from the diagonalized hyperfine structure tensor elements via $A'_x = \frac{A_x}{hc}$ etc. with Planck's constant h and the speed of light c .

Sample	g_{\perp}	g_{\parallel}	A'_{\perp} / MHz	A'_{\parallel} / MHz	g_{Rad1}	g_{Rad2}	g_{Rad3}	g_{Rad4}
ZC3873090	2.082	2.320	153	516	-	2.004	-	-
Z0873090	-	-	-	-	2.036	2.004	1.967	1.958

As the simulation fits with the experimental spectrum, it is concluded that the main part of the Cu^{2+} ions are in axial configuration. However, it cannot clearly be determined which Cu^{2+} ions are giving the origin of the EPR signal, whether the Cu^{2+} ions belonging to CuO or those which are substituting Zn^{2+} ions on its sites.

In the latter case, the Cu^{2+} ions would have a tetrahedral configuration on its sites in the wurtzite structure. In an ideal case, tetrahedral configuration would create an isotropic symmetry and an isotropic EPR signal. However, as listed in Table 1, the c/a ratio measured by XRD was different from the ideal value. Hence, the Cu^{2+} ions are found in axial symmetry.

The substitution is possible, as the ionic radius for Cu^{2+} with coordination number (CN) $CN = 4$, $r_{Cu^{2+}} = 0.057$ nm, is very close to the ionic radius for Zn^{2+} with $CN = 4$, $r_{Zn^{2+}} = 0.060$ nm [36]. A similar EPR signal for Cu^{2+} ions, that substitute Zn^{2+} ions in the ZnO matrix, was also reported by Elirassi and Chandrasekaran [2,25] and Elirassi *et al.* [26]. However, as it is seen in the XRD results, the sample contains also the CuO phase. CuO has a monoclinic crystal structure with C2/2 symmetry [37]. Therefore, Cu^{2+} ions in CuO are

surrounded by oxygen ions in octahedral configuration. Hence, the Cu^{2+} ions in CuO could also give the origin of the anisotropic EPR signal.

The temperature dependence of the signal intensity associated to Cu^{2+} is due to changes in the magnetic coupling between the Cu^{2+} ions. It is why we can plot $1/Area$ Vs temperature and determine if the coupling is ferromagnetic or other ordering phase. The intensity is proportional to the area of one signal and it was evaluated by double integration of the spectrum between 260 mT and 360 mT. The area from the radicals signals, evaluated between 335 mT and 338 mT, was subtracted from the total integration area of the previous step. The inverse of the intensity, $1/Area$, vs. temperature, T , is shown in Figure 6 a and b for samples calcinated at 823 K and 873 K respectively. A linear fit of this curve and the use of the Curie-Weiss law [1,38]

$$I(T) = \frac{C}{T - \Theta_C} \quad (7)$$

allows the determination of the Curie-Weiss temperature Θ_C , where C is the Curie constant multiplied with the proportionality factor between I and the magnetic

susceptibility χ . The linear fit for ZC3823 sample at $T > 210$ K is shown in Figure 6a and in figure 6b for ZC3873 sample at $T > 250$ K. In this last figure a plateau is observed below this temperature. From figure 6a a negative value of T_C is obtained. This negative value indicates that the Cu-ZnO suffers a transition to an anti-ferromagnetic or ferrimagnetic state at low temperatures. So, now it is necessary adjust the curve with the equation

$$I(T) = \frac{C}{T + T_N} \quad (8)$$

where T_N is the Néel-temperature and C has the same meaning like in Eq. 7. $T_N = 139$ K is obtained showing that the Cu^{2+} ions are not strongly magnetically coupled, so that above $T_N = 139$ K the material is paramagnetic. However, when the sample is cooled below $T_N = 139$ K, a transition to anti-ferromagnetism or ferrimagnetism is expected. In contrast, in the fit for ZC3873 a Curie temperature value of $\Theta_C = 137$ K is obtained. This indicates that the Cu^{2+} ions for the sample with $T_C = 873$ K are ferromagnetically coupled.

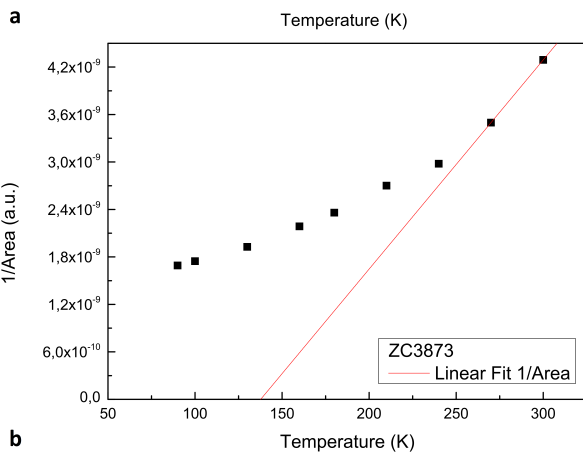
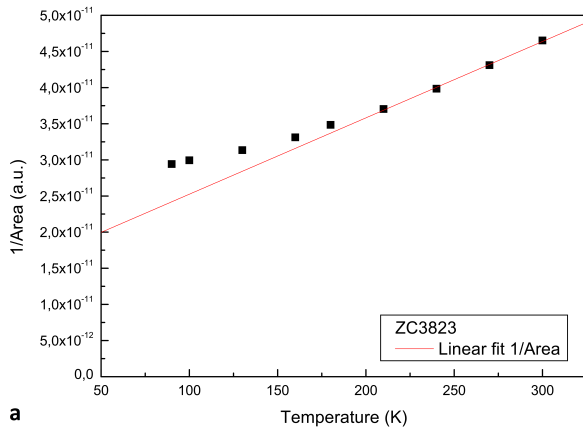


Figure 6. Inverse EPR line intensity of the Cu^{2+} ion depending on temperature for (a) ZC3823, (b) ZC3873.

III.4. UV-DRS Results

UV-Vis spectra for samples calcinated at $T_c = 873$ K, in the range from 300 nm to 800 nm, are showed in Figure 7. The small absorption ranging from 350-500 nm corresponds

to interband transition of ZnO. In case of Cu-doped ZnO samples, it is observed a broad absorption peaks around 600-800 nm associated with $d-d$ transition of Cu^{2+} ions, in addition to ZnO band to band transition [39].

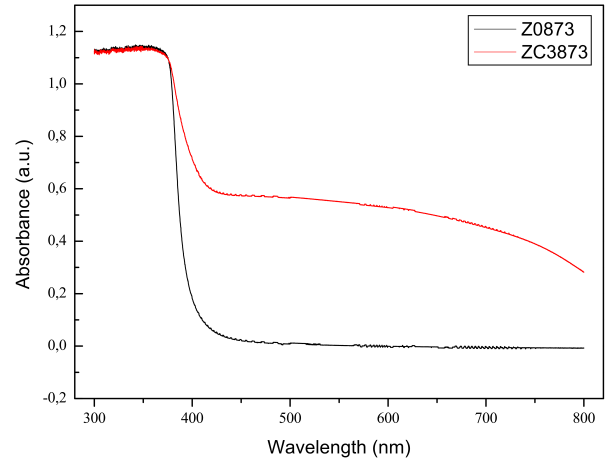


Figure 7. UV-vis spectra for Z0873 (black) and ZC3873 (red).

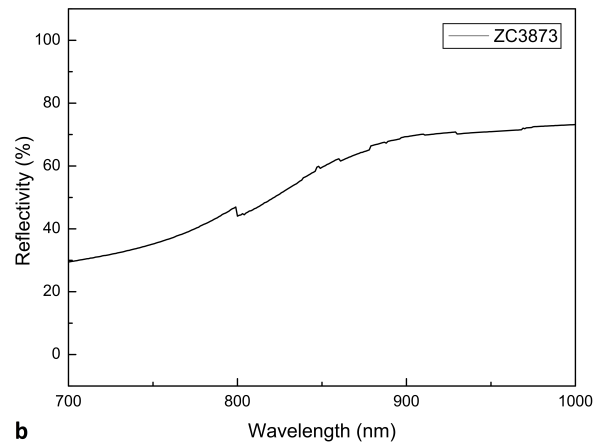
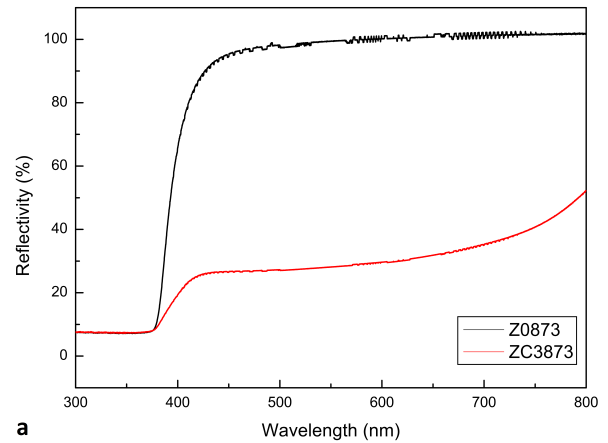


Figure 8. (a) DRS spectra for Z0823 (black) and ZC3823 (red). (b) DRS spectra for ZC3873 sample where signal associated with copper oxide is shown.

The DRS spectra for Z0823 and ZC3873 are shown in Figure 8. The spectra for the other samples studied have similar shape.

In order to determine the band gap E_g of the samples, the DRS data were converted using the Kubelka-Munk equation [40]

$$\frac{k}{s} = \frac{(1 - R)^2}{2R} = f(R) \quad (9)$$

where k is an absorption coefficient, s a scattering coefficient and R the measured reflectivity.

The values of Eq. 9 can be used to extract the (optical) band gap of the samples graphically. This is done using a modified Tauc plot, where $\left(\frac{k}{s} \cdot hv\right)^2$ is plotted against hv . This is shown in Figure 9a for the sample Z0873 and Figure 9b for CuO formed in ZC3873 sample.

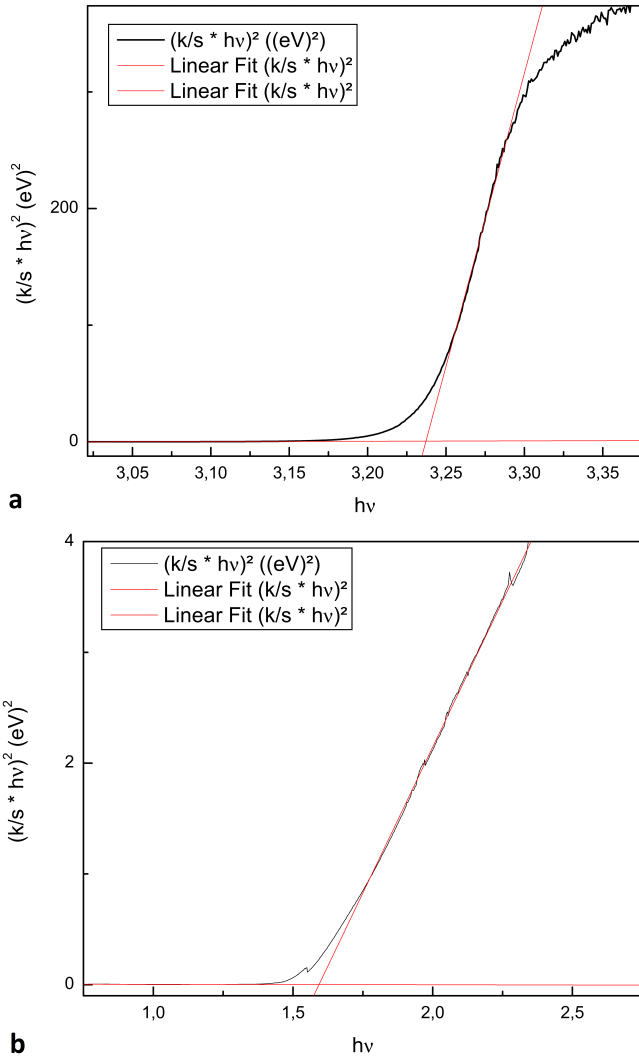


Figure 9. Tauc plots for (a) Z0873 sample. (b) ZC3873 sample.

The measured values of E_g vs. T_C are shown in Figure 10 and in Table 3.

It is seen that the Cu-doped samples have a lower band gap than the pure ZnO samples. Furthermore, the band gap of the $Zn_{0.97}Cu_{0.03}O$ samples decreases significantly with T_C .

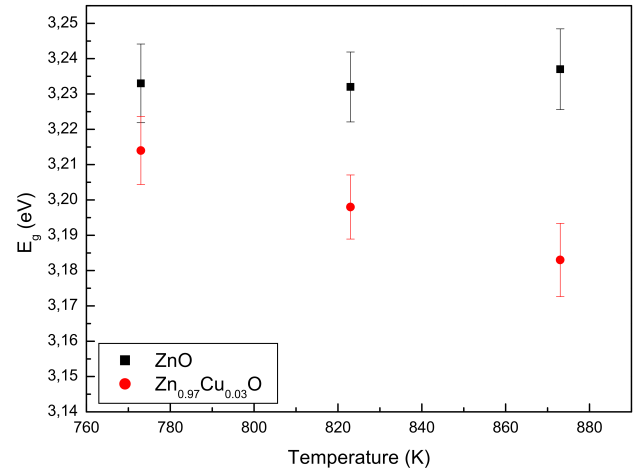


Figure 10. Measured band gap for ZnO by DRS.

A band gap at $E_g \approx 1.6 eV$ was measured in the Cu-containing samples (see Table 3), which is connected to CuO with a band gap of 1.2-1.9 eV [37]. That confirms that some of the introduced Cu^{2+} did not enter the ZnO matrix but formed a CuO phase. That confirms that a small quantity of CuO was formed. However, since E_g related to ZnO lowered with Cu-doping, introduction of Cu atoms in ZnO matrix reduced the band gap. It has been observed by other authors in other materials, as well [39].

IV. CONCLUSION

The experiments show that ZnO nanoparticles with wurtzite phase were synthesized by the sol-gel method. The measured size of the nanoparticles is smaller with $x = 3$ at.% Cu-content than for the pure ZnO samples. However, XRD measurements and the measured band gap by DRS at $E_g \approx 1.6 eV$ revealed the presence of CuO in the Cu-containing samples. In consequence, not all of the Cu^{2+} ions entered the ZnO matrix. However, as the measured band gap by DRS for ZnO was smaller for the Cu-containing samples, it can be concluded, that a part of the Cu^{2+} ions was incorporated in the ZnO matrix and reduced the band gap of the ZnO. Furthermore, the way in which Cu^{2+} ions enter the ZnO samples could be different for the different T_C , as both the band gap for the Cu-containing samples was lower with increasing T_C as the magnetic behavior. The EPR measurements for the sample with $T_C = 873 K$ show Cu^{2+} ions in axial symmetry, which was confirmed by the simulation with an anisotropic Hamiltonian using the g tensor values $g_{\perp} = 2.082$ and $g_{\parallel} = 2.320$. It cannot be said that Cu EPR signal is due to Cu^{2+} ions in the CuO phase or due to Cu^{2+} ions substituting Zn^{2+} ions in the ZnO phase, as for both possibilities Cu^{2+} would have an axial configuration. Investigation of the EPR signal intensity depending on the measurement temperature showed that the Cu^{2+} ions in the Cu-containing samples are ferromagnetically coupled when they are calculated at 873 K. This transition from paramagnetism to ferromagnetism is characterized by the measured Curie temperature $\Theta_C = 137 K$. If the samples are prepared at 823 K the magnetic behavior is

anti-ferromagnetism or ferrimagnetism at temperature lower than 139 K. When magnetic properties of DMS are studied, the obtained results should be taken into account, as the properties do not only depend on the incorporated material, but also on the manner how they enter the matrix or if they form a separate phase and on the calcination temperature T_C .

V. ACKNOWLEDGEMENT

We thank the DIB of the National University of Colombia for the financial support along the project with the code 15848. Additionally, we thank Prof. Mario Barrera for providing the equipment and laboratories used for the material synthesis.

Table 3. Measured band gap E_g by DRS. The Cu-containing samples show a gap related to ZnO ($E_g \approx 3.2 \text{ eV}$) and a gap related to CuO ($E_g \approx 1.6 \text{ eV}$).

T_C (K)	Gap ZnO (eV)	Error(%)	Gap $\text{Zn}_{0.97}\text{Cu}_{0.03}\text{O}$ (nm)	Error(%)	Gap CuO (nm)	Error(%)
773	3.233	1.11	3.214	0.96	1.563	0.51
823	3.232	0.99	3.198	0.91	1.548	0.78
873	3.237	1.14	3.183	1.04	1.593	0.50

REFERENCES

- [1] F. Acosta-Humánez, R. Cogollo Pitalúa and O. Almanza, *Journal of Magnetism and Magnetic Materials* 329, 39 (2013).
- [2] R. Elilarassi and G. Chandrasekaran, *Frontiers of Materials Science* 7, 196 (2013).
- [3] S. Singhal, J. Kaur, T. Namgyal and R. Sharma, *Physica B: Condensed Matter* 407, 1223 (2012).
- [4] A. J. Reddy, M. Kokila, H. Nagabhushana, R. Chakradhar, C. Shivakumara, J. Rao and B. Nagabhushana, *Journal of Alloys and Compounds* 509, 5349 (2011).
- [5] F. Meng, J. Yin, Y.-Q. Duan, Z.-H. Yuan and L.-J. Bie, *Sensors and Actuators B: Chemical* 156, 703 (2011).
- [6] Z. Liu, C. Liu, J. Ya and E. Lei, *Renewable Energy* 36, 1177 (2011).
- [7] K. Hembram, D. Sivaprahasam and T. N. Rao, *Journal of the European Ceramic Society* 31, 1905 (2011).
- [8] Y. Ryu, T.-S. Lee, J. A. Lubguban, H. W. White, B.-J. Kim, Y.-S. Park and C.-J. Youn, *Applied Physics Letters* 88, 241108 (2006).
- [9] N. Daneshvar, D. Salari and A. R. Khataee, *Journal of Photochemistry and Photobiology A: Chemistry* 162, 317 (2004).
- [10] N. Jones, B. Ray, K. T. Ranjit and A. C. Manna, *FEMS microbiology letters* 279, 71 (2008).
- [11] L. Zhang, Y. Jiang, Y. Ding, M. Povey and D. York, *Journal of Nanoparticle Research* 9, 479 (2007).
- [12] M. Premanathan, K. Karthikeyan, K. Jeyasubramanian and G. Manivannan, *Nanomedicine: Nanotechnology, Biology and Medicine* 7, 184 (2011).
- [13] C. Hanley, J. Layne, A. Punnoose, K. M. Reddy, I. Coombs, A. Coombs, K. Feris and D. Wingett, *Nanotechnology* 19, 295103 (2008).
- [14] T. Minami, *Semiconductor Science and Technology* 20, S35 (2005).
- [15] F. Pan, C. Song, X. J. Liu, Y. C. Yang and F. Zeng, *Materials Science and Engineering R: Reports* 62, 1 (2008).
- [16] S. French, A.A. Sokol, S. Bromley, C. Catlow and P. Sherwood, *Topics in Catalysis* 24, 161 (2003).
- [17] U. S. U. Thampy, C. R. Krishna, C. V. Reddy, B. Babu, Y. P. Reddy, P. S. Rao and R. V. S. S. N. Ravikumar, *Applied Magnetic Resonance* 41, 69 (2011).
- [18] R. N. Aljawfi and S. Mollah, *Journal of Magnetism and Magnetic Materials* 323, 3126 (2011).
- [19] A. O. Ankiewicz, M. C. Carmo, N. A. Sobolev, W. Gehlhoff, E. M. Kaidashev, A. Rahm, M. Lorenz and M. Grundmann, *Journal of Applied Physics* 101, 024324 (2007).
- [20] A. Jagannatha Reddy, M. K. Kokila, H. Nagabhushana, C. Shivakumara, R. P. S. Chakradhar, B. M. Nagabhushana and R. Hari Krishna, *Spectrochimica Acta Part A: Molecular and biomolecular spectroscopy* 132, 305 (2014).
- [21] H. Liu, J. Yang, Z. Hua, Y. Zhang, L. Yang, L. Xiao and Z. Xie, *Applied Surface Science* 256, 4162 (2010).
- [22] T. Saidani, M. Zaabat, M. S. Aida, A. Benaboud, S. Benzitouni and A. Boudine, *Superlattices and Microstructures* 74, 47 (2014).
- [23] M. Fu, Y. Li, S. Wu, P. Lu, J. Liu and F. Dong, *Applied Surface Science* 258, 1587 (2011).
- [24] A. Iribarren, E. Hernández-Rodríguez and L. Maqueira, *Materials Research Bulletin* 60, 376 (2014).
- [25] R. Elilarassi and G. Chandrasekaran, *Journal of Materials Science: Materials in Electronics* 21, 1168 (2010).
- [26] R. Elilarassi, P. Sambasiva Rao and G. Chandrasekaran, *Journal of Sol-Gel Science and Technology* 57, 101 (2011).
- [27] B. Babu, T. Aswani, G. Thirumala Rao, R. Joyce Stella, B. Jayaraja and R.V.S.S.N. Ravikumar, *Journal of Magnetism and Magnetic Materials* 355, 76 (2014).
- [28] Rodríguez-Carvajal, J. *Fullprof Suite* (2012).
- [29] S. Stoll and A. Schweiger, *Journal of Magnetic Resonance* 178, 42 (2006).
- [30] K. Norrish and R. M. Taylor, *Clay minerals bulletin* 5 (28), 98 (1962).
- [31] Y. Waseda, E. Matsubara and K. Shinoda, *X-Ray Diffraction Crystallography* (Springer-Verlag, Berlin Heidelberg, (2011) pp. 123-127.
- [32] A. J. Hashim, M. S. Jaafar, A. J. Ghazai and N. M. Ahmed, *Optik* 124, 491 (2013).

- [33] G. Gottstein, *Physikalische Grundlagen der Materialkunde*, 4th edition (Berlin Heidelberg, 2014), pp. 1-4.
- [34] L. S. Vlasenko and G. D. Watkins, *Physical Review B* 72, 1 (2005).
- [35] L. S. Vlasenko, *Applied Magnetic Resonance* 39,103 (2010).
- [36] R. D. Shannon, *Acta Crystallographica Section A: Crystal Physics, Diffraction, Theoretical and General Crystallography* 32, 751 (1976).
- [37] D. Wu, Q. Zhang and M. Tao, *Physical Review B: Condensed Matter and Materials Physics* 73, 1 (2006).
- [38] A. Mauger, *Applied Magnetic Resonance* 39, 3 (2010).
- [39] S. Anandan, N. Ohashi and M. Miyauchi, *Applied Catalysis B: Environmental* 100, 502 (2010).
- [40] A. Murphy, *Solar Energy Materials & Solar Cells* 91, 1326 (2007).